

# A Neural-Network-Based Convex Regularizer for Image Reconstruction

Alexis Goujon, Sebastian Neumayer, Pakshal Bohra, Stanislas Ducotterd, and Michael Unser

**Abstract**—The emergence of deep-learning-based methods for solving inverse problems has enabled a significant increase in reconstruction quality. Unfortunately, these new methods often lack reliability and explainability, and there is a growing interest to address these shortcomings while retaining the performance. In this work, this problem is tackled by revisiting regularizers that are the sum of convex-ridge functions. The gradient of such regularizers is parametrized by a neural network that has a single hidden layer with increasing and learnable activation functions. This neural network is trained within a few minutes as a multi-step Gaussian denoiser. The numerical experiments for denoising, CT, and MRI reconstruction show improvements over methods that offer similar reliability guarantees.

## I. INTRODUCTION

In natural science, it is common to probe indirectly an object of interest by collecting a series of linear measurements [1]. After discretization, this measurement scheme is formalized as

$$\mathbf{y} = \mathbf{H}\mathbf{x} + \mathbf{n}, \quad (1)$$

where  $\mathbf{H} \in \mathbb{R}^{m \times d}$  acts on a discrete object representation  $\mathbf{x} \in \mathbb{R}^d$  and models the physics of the process. The vector  $\mathbf{n} \in \mathbb{R}^m$  accounts for additive noise in the measurements. Given the measurement vector  $\mathbf{y}$ , the task is then to reconstruct  $\mathbf{x}$ . Many medical imaging applications fit into this class of inverse problems [2], including magnetic resonance imaging (MRI) and X-ray computed tomography (CT).

In addition to the noise—which makes the reconstruction challenging for ill-conditioned  $\mathbf{H}$ —it is common to have only a few measurements ( $m < d$ ), resulting in underdetermined problems. In both cases, the problems are ill-posed, and solving them poses serious challenges. To overcome this issue, the reconstruction is often computed as

$$\arg \min_{\mathbf{x} \in \mathbb{R}^d} \|\mathbf{H}\mathbf{x} - \mathbf{y}\|_2^2 + R(\mathbf{x}), \quad (2)$$

where  $R: \mathbb{R}^d \rightarrow \mathbb{R}$  is a convex regularizer that incorporates prior information about  $\mathbf{x}$  to counteract the ill-posedness of the problem. Popular choices are the Tikhonov [3] or total-variation (TV) [4]–[6] regularizers.

### A. Deep-learning Methods

Deep-learning-based reconstruction methods have emerged in the past years for inverting (1) in a variety of applications; see [7], [8] for an overview. Such methods offer significantly

improved reconstruction quality compared to classical variational models of the form (2). Unfortunately, most of these deep-learning-based methods are not well understood and lack stability guarantees [9], [10].

For end-to-end approaches, a pre-trained model outputs the reconstruction  $\mathbf{x}$  directly from the measurements  $\mathbf{y}$  or from a low-quality reconstruction [11]–[15]. These approaches are often much faster than the classical iterative solvers to compute (2). Their downside is that they offer no control of the data consistency  $\|\mathbf{H}\mathbf{x} - \mathbf{y}\|_2$ . Further, they are less universal since a model is specifically trained for one operator  $\mathbf{H}$  and one noise model. Potentially, end-to-end learning can even lead to serious stability issues [9].

A remedy for some of these issues is provided by the convolutional neural network (CNN) variants of the Plug-and-Play (PnP) framework [16]–[19]. The inspiration for these methods comes from the interpretation of the proximal operator

$$\text{prox}_R(\mathbf{y}) = \arg \min_{\mathbf{x} \in \mathbb{R}^d} \frac{1}{2} \|\mathbf{y} - \mathbf{x}\|_2^2 + R(\mathbf{x})$$

used in many iterative algorithms for computing (2) as a denoiser. The idea then is to replace the latter with a more powerful CNN-based denoiser  $D$ . However,  $D$  is usually not a proper proximal operator, and the convergence of the PnP iterates is not granted. It was shown in [19] that for an invertible  $\mathbf{H}$ , convergence can be ensured by constraining the Lipschitz constant of the residual operator  $(I - D)$ . For a non-invertible  $\mathbf{H}$ , this constraint, however, does not suffice. Instead, one can constrain  $D$  to be an averaged operator, which unfortunately degrades the performances [20]. Hence, in practice, one usually only constrains  $(I - D)$  even if the framework is deployed for non-invertible  $\mathbf{H}$  [19], [21], [22]. While this results in good performances, it leaves a gap between theory and implementation. Following a different route, convergence can also be ensured with relaxed algorithms [23], [24]. There,  $D$  is replaced by the relaxed version  $\gamma D + (1 - \gamma)I$ ,  $\gamma \in (0, 1]$ . At each iteration,  $\gamma$  is decreased if some condition is violated. Unfortunately, with no constraints on  $D$ , the evolution of  $\gamma$  is unpredictable. Hence, the associated fixed point equation for the reconstruction is a priori unknown, which reduces the reliability of the method.

Another data-driven approach arising from (2) is learning the regularizer  $R$  instead of its proximal operator. Pioneering work in this direction includes the Field of Experts [25]–[27], where  $R$  is parametrized by an interpretable and shallow model; namely a sum of nonlinear one-dimensional functions composed with convolutional filters. Some recent approaches rely on more sophisticated architectures with much deeper

\*The authors are with the Biomedical Imaging Group, École Polytechnique Fédérale de Lausanne (EPFL), Station 17, CH-1015 Lausanne, {firstname.name}@epfl.ch.

CNNs, such as with the adversarial regularization [28], [29], the NETT [30] and the total deep variation [31] frameworks, or with regularizers for which a proximal operator exist [24], [32]–[34]. There exist a variety of strategies to learn  $R$ , including bilevel optimization [26], unrolling [27], [31], gradient-step denoising [24], [32] and adversarial training [28], [29]. When  $R$  is convex, a global minimizer of (2) can be found under mild assumptions. Relaxing the convexity constraint usually boosts the performance [26], [35], and it is consequently the most popular approach. Unfortunately, one can then only expect convergence to a critical point.

### B. The Quest for Reliability

In many sensitive applications, such as medical imaging, there is a growing interest to improve the reliability and interpretability of the reconstruction method. The available frameworks used to learn a (pseudo) proximal operator or regularizer result in a variety of neuronal architectures that differ in the importance attributed to the following competing properties:

- good reconstruction quality;
- independence on  $\mathbf{H}$ , noise model and image domain;
- convergence guarantees and properties of the fixed points of the reconstruction algorithm;
- interpretability, which can include the existence of an explicit cost or a minimal understanding of what the regularizer is promoting.

To promote the last two properties, one usually has to impose structural constraints on the learnt regularizer/proximal operator. For instance, within the PnP framework, there have been some recent efforts to improve the expressivity of averaged denoisers, either with strict Lipschitz constraints on the model, [20], [36] or with regularization of its Lipschitz constant during training [33], [37], which in turn improves the convergence properties of the reconstruction algorithm. In the same vein, [38], [39] proposed to learn a convex regularizer parametrized by a deep input convex neural network (ICNN) [40] and to train it within the adversarial framework introduced in [28].

In the present work, we prioritize the reliability and interpretability of the method. Thus, we revisit the family of learnable convex-ridge regularizers [25]–[27], [35], [41]

$$R: \mathbf{x} \mapsto \sum_i \psi_i(\mathbf{w}_i^T \mathbf{x}), \quad (3)$$

where the profile functions  $\psi_i: \mathbb{R} \rightarrow \mathbb{R}$  are convex. A popular way to learn  $R$  is to solve a nonconvex bi-level optimization task [42], [43] for a given inverse problem. It was reported in [26] that these learnt regularizers outperform the popular TV regularizer for image reconstruction. As bi-level optimization is computationally quite intensive, it was proposed in [35] to unroll the forward-backward splitting (FBS) algorithm applied to (2) with a regularizer of the form (3). Accordingly,  $R$  is optimized so that a predefined number  $t$  of iterations of the FBS algorithm yields a good reconstruction. Unfortunately, on a denoising task with learnable profile functions  $\psi_i$ , the proposed approach does not match the performance of the bi-level optimization. To deal with these shortcomings, we introduce

an efficient framework to learn a convex-ridge regularizer with free-form convex profile functions. We train this regularizer on a generic denoising task and then plug it into (2). This yields a generic reconstruction framework that is applicable to a variety of inverse problems. The main contributions of the present work are as follows.

- **Interpretable and expressive model:** We use a one-hidden-layer neural network (NN) with learnable increasing linear-spline activation functions to parametrize the gradient of the regularizer. We prove that this yields the maximum expressivity in the generic setting (3);
- **Embedding of the constraints into the forward pass:** The structural constraints on the model are embedded into the forward pass during the training. This includes an efficient procedure to enforce the convexity of the profile functions, and the computation of a bound on the Lipschitz constant of  $\nabla R$ , which is required for our training procedure;
- **Ultra-fast training:** The regularizer is learnt via the training of a multi-gradient-step denoiser. Empirically, we observe that a few gradient steps suffice to learn a best-performing regularizer. This leads to training within a few minutes;
- **Best reconstruction quality in a constrained scenario:** We show that our framework outperforms recent deep-learning-based approaches with comparable guarantees and constraints in two popular medical imaging modalities (CT and MRI). This includes the PnP method with averaged denoisers and a variational framework with a learnable deep convex regularizer. This even holds for a strong mismatch in the training and testing noise levels.

## II. ARCHITECTURE OF THE REGULARIZER

In this section, we introduce the notions required to define the convex-ridge regularizer neural network (CRR-NN).

### A. General Setting

Our goal is to learn a regularizer  $R$  for the variational problem (2) that performs well across a variety of ill-posed problems. Similar to the PnP framework, we view the denoising task

$$\mathbf{x}^* = \arg \min_{\mathbf{x} \in \mathbb{R}^d} \frac{1}{2} \|\mathbf{x} - \mathbf{y}\|_2^2 + \lambda R(\mathbf{x}), \quad (4)$$

as the underlying base problem for training, where  $\mathbf{y}$  is the noisy image. Since we prioritize interpretability and reliability, we choose the simple convex-ridge regularizer (3). More precisely, we use a convolutional form

$$R: \mathbf{x}_{2d} \mapsto \sum_{n=1}^{N_C} \sum_{\mathbf{k}} \psi_n((\mathbf{h}_n * \mathbf{x}_{2d})[\mathbf{k}]), \quad (5)$$

where  $\mathbf{x}_{2d}$  represents a 2D image, the  $\mathbf{h}_n$  represent 2D convolution kernels, and  $N_C$  is the number of channels. Since (5) is a special case of (3), we henceforth use the generic form to simplify the notations. Further, we use the notation  $R_\theta$  to express the dependence of  $R$  on the aggregated set of learnable parameters  $\theta$ , which shall be specified when necessary. In the

sequel, we assume that the convex profile functions  $\psi_i$  have a Lipschitz continuous derivative, i.e.  $\psi_i \in C^{1,1}(\mathbb{R})$ .

### B. Gradient-Step Neural Network

Given the assumptions on  $R_\theta$ , the denoised image in (4) can be interpreted as the unique fixed point of  $\mathbf{T}_{R_\theta, \lambda, \alpha}: \mathbb{R}^d \rightarrow \mathbb{R}^d$  defined by

$$\mathbf{T}_{R_\theta, \lambda, \alpha}(\mathbf{x}) = \mathbf{x} - \alpha((\mathbf{x} - \mathbf{y}) + \lambda \nabla R_\theta(\mathbf{x})). \quad (6)$$

Iterating (6) implements a gradient descent with stepsize  $\alpha$ , which converges if  $\alpha \in (0, 2/(1 + \lambda L_\theta))$  where  $L_\theta = \text{Lip}(\nabla R_\theta)$  is the Lipschitz constant of  $\nabla R_\theta$ . In the sequel, we always enforce this constraint on  $\alpha$ . The gradient of the generic convex-ridge expression (3) is given by

$$\nabla R_\theta(\mathbf{x}) = \mathbf{W}^T \boldsymbol{\sigma}(\mathbf{W}\mathbf{x}), \quad (7)$$

where  $\mathbf{W} = [\mathbf{w}_1 \cdots \mathbf{w}_p]^T \in \mathbb{R}^{p \times d}$  and  $\boldsymbol{\sigma}$  is a pointwise activation function whose components  $(\sigma_i = \psi'_i)_{i=1}^p$  are Lipschitz continuous and increasing. In our implementation, the activation functions  $\sigma_i$  are shared within each channel of  $\mathbf{W}$ . The resulting gradient-step operator

$$\mathbf{T}_{R_\theta, \lambda, \alpha}(\mathbf{x}) = (1 - \alpha)\mathbf{x} + \alpha(\mathbf{y} - \lambda \mathbf{W}^T \boldsymbol{\sigma}(\mathbf{W}\mathbf{x})) \quad (8)$$

corresponds to a one-hidden-layer convolutional NN with a bias and a skip connection, and we refer to it as a **gradient-step NN**. The training of a gradient-step NN will give a CRR-NN.

## III. CHARACTERIZING GOOD PROFILE FUNCTIONS

In this section, we provide theoretical results to motivate our choice of the profile functions  $\psi_i$  or, equivalently, of their derivatives  $\sigma_i = \psi'_i$ . This will lead us to the implementation presented in Section IV.

### A. Ensuring the Existence of Minimizers

The convexity of  $R_\theta$  is not sufficient to ensure that the solution set (2) is nonempty for a non-invertible forward matrix  $\mathbf{H}$ . With convex-ridge regularizers, this shortcoming can be addressed under a mild condition on the functions  $\psi_i$  (Proposition III.1). The implications for our implementation are detailed in Section IV-B.

**Proposition III.1.** *Let  $\mathbf{H} \in \mathbb{R}^{m \times d}$  and  $\psi_i: \mathbb{R} \rightarrow \mathbb{R}$ ,  $i = 1, \dots, p$ , be convex functions. If  $\arg \min_{t \in \mathbb{R}} \psi_i(t) \neq \emptyset$  for all  $i = 1, \dots, p$ , then*

$$\emptyset \neq \arg \min_{\mathbf{x} \in \mathbb{R}^d} \|\mathbf{H}\mathbf{x} - \mathbf{y}\|_2^2 + \sum_{i=1}^p \psi_i(\mathbf{w}_i^T \mathbf{x}). \quad (9)$$

*Proof.* Set  $S_i = \arg \min_{t \in \mathbb{R}} \psi_i(t)$ . Then, each convex ridge  $\psi_i(\mathbf{w}_i^T \cdot)$  partitions  $\mathbb{R}^d$  into the three (possibly empty) convex polytopes:

- $\Omega_0^i = \{\mathbf{x} \in \mathbb{R}^d : \mathbf{w}_i^T \mathbf{x} \in S_i\}$ ;
- $\Omega_1^i = \{\mathbf{x} \in \mathbb{R}^d : \mathbf{w}_i^T \mathbf{x} \leq \inf S_i\}$ ;
- $\Omega_2^i = \{\mathbf{x} \in \mathbb{R}^d : \mathbf{w}_i^T \mathbf{x} \geq \sup S_i\}$ .

Based on these, we partition  $\mathbb{R}^d$  into finitely many polytopes of the form  $\bigcap_{i=1}^p \Omega_{m_i}^i$ , where  $m_i \in \{0, 1, 2\}$ . The infimum of

the objective in (9) must be attained in at least one of these polytopes, say  $P = \bigcap_{i=1}^p \Omega_{m_i}^i$ .

Now, we pick a minimizing sequence  $(\mathbf{x}_k)_{k \in \mathbb{N}} \subset P$ . Let  $\mathbf{M}$  be the matrix whose rows are the rows of  $\mathbf{H}$  and the  $\mathbf{w}_i^T$  with  $m_i \neq 0$ . Due to the coercivity of  $\|\cdot\|_2^2$ , we get that  $\mathbf{H}\mathbf{x}_k$  remains bounded. As the  $\psi_i$  are convex, they are coercive on the intervals  $(-\infty, \inf S_i]$  and  $[\sup S_i, +\infty)$ , and hence also  $\mathbf{w}_i^T \mathbf{x}_k$  remains bounded. Therefore, the sequence  $(\mathbf{M}\mathbf{x}_k)_{k \in \mathbb{N}}$  is bounded, and we can drop to a convergent subsequence with limit  $\mathbf{u} \in \text{ran}(\mathbf{M})$ . The associated set

$$Q = \{\mathbf{x} \in \mathbb{R}^d : \mathbf{M}\mathbf{x} = \mathbf{u}\} = \{\mathbf{M}^\dagger \mathbf{u}\} + \ker(\mathbf{M})$$

is a closed affine space, i.e. a closed polytope. It holds that

$$\begin{aligned} \text{dist}(\mathbf{x}_k, Q) &= \text{dist}(\mathbf{M}^\dagger \mathbf{M}\mathbf{x}_k + \text{P}_{\ker(\mathbf{M})}(\mathbf{x}_k), Q) \\ &\leq \text{dist}(\mathbf{M}^\dagger \mathbf{M}\mathbf{x}_k, \mathbf{M}^\dagger \mathbf{u}) \rightarrow 0 \end{aligned} \quad (10) \quad (11)$$

as  $k \rightarrow +\infty$ , and thus  $\text{dist}(P, Q) = 0$ . The distance of closed polytopes  $P$  and  $Q$  is 0 if and only if  $P \cap Q \neq \emptyset$  [44, Theorem 1]. Note that  $\psi_i(\mathbf{w}_i^T \cdot)$  is constant on  $P$  if  $m_i = 0$ . Hence, any  $\mathbf{x} \in P \cap Q$  is a minimizer of (9).  $\square$

The proof of Proposition III.1 directly exploits the properties of ridge functions. Whether it is possible to extend the result to more complex or even generic convex regularizers is not known to the authors. Note that the assumption in Proposition III.1 is rather weak as neither the cost function nor the one-dimensional profiles  $\psi_i$  need to be coercive.

### B. Expressivity of Profile Functions

The gradient-step NN  $\mathbf{T}_{R_\theta, \lambda, \alpha}$  introduced in (8) is the key component of our training procedure. Here, we investigate its expressivity depending on the choice of the activation functions  $\sigma_i$  for parametrizing  $\nabla R_\theta$ .

Let  $C_{\uparrow}^{0,1}(\mathbb{R})$  be the set of scalar Lipschitz continuous and increasing functions on  $\mathbb{R}$ , and let  $\mathcal{LS}_{\uparrow}^m(\mathbb{R})$  be the subset of increasing linear splines with at most  $m$  knots. We also define

$$\mathcal{E}(\mathbb{R}^d) = \{\mathbf{W}^T \boldsymbol{\sigma}(\mathbf{W}\cdot) : \mathbf{W} \in \mathbb{R}^{p \times d}, \sigma_i \in C_{\uparrow}^{0,1}(\mathbb{R})\}, \quad (12)$$

and, further, for any  $\Omega \subset \mathbb{R}^d$

$$\mathcal{E}(\Omega) = \{\mathbf{f}|_{\Omega} : \mathbf{f} \in \mathcal{E}(\mathbb{R}^d)\}. \quad (13)$$

In the following, we use  $\|\mathbf{f}\|_{C(\Omega)} := \sup_{\mathbf{x} \in \Omega} \|\mathbf{f}(\mathbf{x})\|$  and  $\|\mathbf{f}\|_{C^1(\Omega)} := \sup_{\mathbf{x} \in \Omega} \|\mathbf{f}(\mathbf{x})\| + \sup_{\mathbf{x} \in \Omega} \|\mathbf{J}_{\mathbf{f}}(\mathbf{x})\|$ .

The popular ReLU activation function is Lipschitz continuous and increasing. Unfortunately, it comes with limited expressivity as shown in Proposition III.2.

**Proposition III.2.** *Let  $\Omega \subset \mathbb{R}^d$  be compact with a nonempty interior. Then, the set*

$$\{\mathbf{W}^T \text{ReLU}(\mathbf{W}\cdot - \mathbf{b}) : \mathbf{W} \in \mathbb{R}^{p \times d}, \mathbf{b} \in \mathbb{R}^p\} \quad (14)$$

*is not dense with respect to  $\|\cdot\|_{C(\Omega)}$  in  $\mathcal{E}(\Omega)$ .*

*Proof.* Since  $\Omega$  has nonempty interior, there exist  $\mathbf{v} \in \mathbb{R}^d$  with  $\|\mathbf{v}\|_2 = 1$ ,  $a \in \mathbb{R}$  and  $\delta > 0$  such that for  $\mathbf{l}_{\mathbf{v}}: \mathbb{R} \rightarrow \mathbb{R}^d$  with  $\mathbf{l}_{\mathbf{v}}(t) = t\mathbf{v}$ , it holds  $\mathbf{l}_{\mathbf{v}}((a - \delta, a + \delta)) \subset \Omega$ . Now, we prove the

statement by contradiction. If the set (14) is dense in  $\mathcal{E}(\Omega)$ , then the set

$$\begin{aligned} & \{(\mathbf{W}\mathbf{v})^T \text{ReLU}(\mathbf{W}\mathbf{v} \cdot -\mathbf{b}) : \mathbf{W} \in \mathbb{R}^{p \times d}, \mathbf{b} \in \mathbb{R}^p\} \\ &= \left\{ \sum_{i=1}^p w_i \text{ReLU}(w_i \cdot -b_i) : w_i, b_i \in \mathbb{R} \right\} \end{aligned} \quad (15)$$

is dense in  $\mathcal{E}((a-\delta, a+\delta))$ . Note that all functions  $f$  in (14) can be rewritten in the form

$$f(x) = \sum_{i=1}^{p_1} \text{ReLU}(w_i x - b_i) + \sum_{i=1}^{p_2} (-\text{ReLU}(-\tilde{w}_i x - \tilde{b}_i)), \quad (16)$$

where  $w_i, \tilde{w}_i \in \mathbb{R}^+$ ,  $b_i, \tilde{b}_i \in \mathbb{R}$  and  $p_1 + p_2 = p$ . Every summand in this decomposition is an increasing function. For the continuous and increasing function

$$g: t \mapsto \text{ReLU}(t - a + \delta/2) - \text{ReLU}(t - a - \delta/2),$$

the density implies that there exists  $f$  of the form (16) satisfying  $\|g - f\|_{C((a-\delta, a+\delta))} \leq \delta/16$ . Since  $g(a+\delta/2) = g(a+\delta)$ , this implies that  $f(a+\delta) - f(a+\delta/2) \leq \delta/8$ . In addition, it holds that

$$\begin{aligned} & f(a+\delta) - f(a+\delta/2) \\ & \geq \sum_{i=1}^{p_1} \text{ReLU}(w_i(a+\delta) - b_i) - \text{ReLU}(w_i(a+\delta/2) - b_i) \\ & \geq \sum_{\{i: b_i \leq w_i(a+\delta/2)\}} w_i(a+\delta - a - \delta/2) \\ & = \sum_{\{i: b_i \leq w_i(a+\delta/2)\}} w_i \delta/2. \end{aligned} \quad (17)$$

Hence, we conclude that  $\sum_{\{i: b_i \leq w_i(a+\delta/2)\}} w_i \leq 1/4$ . Similarly, we can show that  $\sum_{\{i: -\tilde{b}_i \leq \tilde{w}_i(a-\delta/2)\}} \tilde{w}_i \leq 1/4$ . Using these two estimates, we get

$$\begin{aligned} \frac{7}{8}\delta &= g(a+\delta/2) - g(a-\delta/2) - \frac{1}{8}\delta \\ &\leq f(a+\delta/2) - f(a-\delta/2) \\ &\leq \sum_{\{i: b_i \leq w_i(a+\delta/2)\}} \delta w_i + \sum_{\{i: -\tilde{b}_i \leq \tilde{w}_i(a-\delta/2)\}} \delta \tilde{w}_i \leq \frac{\delta}{2}, \end{aligned} \quad (18)$$

which yields a contradiction. Hence, the set (14) cannot be dense in  $\mathcal{E}(\Omega)$ .  $\square$

In contrast, the set  $\mathcal{E}(\Omega)$  can be approximated using increasing linear-spline activation functions.

**Proposition III.3.** *Let  $\Omega \subset \mathbb{R}^d$  be compact and  $m \geq 2$ . Then, the set*

$$\{\mathbf{W}^T \boldsymbol{\sigma}(\mathbf{W}\cdot) : \mathbf{W} \in \mathbb{R}^{p \times d}, \sigma_i \in \mathcal{LS}_\uparrow^m(\mathbb{R})\} \quad (19)$$

is dense with respect to  $\|\cdot\|_{C(\Omega)}$  in  $\mathcal{E}(\Omega)$ .

*Proof.* First, we consider the case  $d = 1$ . By rescaling and shifting, we can assume that  $S \subset [0, 1]$  without loss of generality. Let  $f \in C_\uparrow^{0,1}([0, 1])$ , and  $\varphi_n$  be the linear-spline interpolator of  $f$  at locations  $0, 1/2^n, \dots, 1-1/2^n, 1$ . Since  $f$  is increasing and  $\varphi_n$  is piecewise linear,  $\varphi_n$  is also increasing. Further, we get

$$\|f - \varphi_n\|_{C([0,1])} \leq \max_{k \in \{1, \dots, 2^n\}} f(k/2^n) - f((k-1)/2^n). \quad (20)$$

As continuous functions on compact sets are uniformly continuous, this directly implies that  $\|f - \varphi_n\|_{C([0,1])} \rightarrow 0$ . Now, we represent  $\varphi_n$  as a linear combination of increasing linear splines with 2 knots

$$\varphi_n(x) = f(0) + \sum_{k=1}^{2^n} a_{k,n} g(2^n \cdot - (k-1)), \quad (21)$$

where  $a_{k,n} = f(k/2^n) - f((k-1)/2^n)$  and  $g$  is given by

$$g(x) = \begin{cases} 0, & x \leq 0 \\ x, & 0 < x \leq 1 \\ 1, & \text{otherwise.} \end{cases} \quad (22)$$

Finally, equation (21) can be recast as  $\varphi_n(x) = \mathbf{w}_n^T \boldsymbol{\sigma}_n(x \mathbf{w}_n)$ , where each  $\boldsymbol{\sigma}_n$  is an increasing linear spline with 2 knots and  $\mathbf{w} \in \mathbb{R}^{2^n}$ . This concludes the proof for  $d = 1$ .

Now, we extend this result to any  $d \in \mathbb{N}^+$ . Let  $\Phi: \mathbb{R}^d \rightarrow \mathbb{R}^d$  be given by  $\mathbf{x} \mapsto \mathbf{W}^T \boldsymbol{\sigma}(\mathbf{W}\mathbf{x})$  with components  $\sigma_i \in C_\uparrow^0(\mathbb{R})$ . Let  $S_i = \{\mathbf{w}_i^T \mathbf{x} : \mathbf{x} \in \Omega\}$ , where  $\mathbf{w}_i \in \mathbb{R}^d$  is the  $i$ th row of  $\mathbf{W}$ . Using the result for  $d = 1$ , each  $\sigma_i$  can be approximated in  $C(S_i)$  by a sequence of functions  $(\mathbf{u}_{n,i}^T \boldsymbol{\varphi}_n(\mathbf{u}_{n,i} \cdot))_{n \in \mathbb{N}}$ , where  $\boldsymbol{\varphi}_n$  has components  $\varphi_{n,i} \in \mathcal{LS}_\uparrow^2(\mathbb{R})$  and  $\mathbf{u}_{n,i}$  are vectors with size independent of  $i$ . Further, the  $\mathbf{u}_{n,i}$  can be chosen such that the  $j$ th component is only nonzero for a single  $i$ . Let  $U_n$  be the matrix whose columns are  $\mathbf{u}_{n,i}$ . Then, we directly have that

$$\lim_{n \rightarrow \infty} \max_{\mathbf{x} \in \{\mathbf{y} \in \mathbb{R}^d : y_i \in S_i\}} \|\mathbf{U}_n^T \boldsymbol{\varphi}_n(\mathbf{U}_n \mathbf{x}) - \boldsymbol{\sigma}(\mathbf{x})\|_2 = 0. \quad (23)$$

Hence, the sequence of function  $((\mathbf{U}_n \mathbf{W})^T \boldsymbol{\varphi}_n(\mathbf{U}_n \mathbf{W} \cdot))_{n \in \mathbb{N}}$  converges to  $\Phi$  in  $C(\Omega)$ . This concludes the proof.  $\square$

In the end, Propositions III.2 and III.3 imply that using linear-spline activation functions instead of the ReLU for the  $\sigma_i$  enables us to approximate strictly more convex regularizers  $R_\theta$ .

**Corollary III.4.** *Let  $\Omega \subset \mathbb{R}^d$  be convex and compact with a nonempty interior. Then, the regularizers of the form (3) with Jacobians of the form (19) are dense in*

$$\left\{ \sum_{i=1}^p \psi_i(\mathbf{w}_i^T \mathbf{x}) : \psi_i \in C^{1,1}(\mathbb{R}) \text{ convex}, \mathbf{w}_i \in \mathbb{R}^d \right\} \quad (24)$$

with respect to  $\|\cdot\|_{C^1(\Omega)}$ . The density does not hold if we only consider regularizers with Jacobians of the form (14).

*Proof.* Let  $R$  be in (24). Consequently, its Jacobian is in  $\mathcal{E}(\Omega)$ . Due to Proposition III.2, the regularizers with Jacobians of the form (14) cannot be dense with respect to  $\|\cdot\|_{C^1(\Omega)}$ . On the other hand, by Proposition III.3, we can pick  $\mathbf{x}_0 \in \Omega$  and corresponding regularizers  $R_n$  of the form (3) with  $\mathbf{J}_{R_n} \in (19)$ ,  $\|\mathbf{J}_{R_n} - \mathbf{J}_R\|_{C(\Omega)} \rightarrow 0$  as  $n \rightarrow \infty$  and  $R_n(\mathbf{x}_0) = R(\mathbf{x}_0)$ . Now, the mean value theorem readily implies  $\|R_n - R\|_{C^1(\Omega)} \rightarrow 0$  as  $n \rightarrow \infty$ .  $\square$

Motivated by these results, we propose to parametrize the  $\sigma_i$  with learnable linear-spline activation functions. This results in profile functions  $\psi_i$  that are splines of degree 2, i.e. piecewise polynomials of degree 2 with continuous derivatives.

#### IV. IMPLEMENTATION

##### A. Training a Multi-Gradient-Step Denoiser

Let  $\{\mathbf{y}^m = \mathbf{x}^m + \mathbf{n}^m\}_{m=1}^M$  be a set of noisy images with clean versions  $\{\mathbf{x}^m\}_{m=1}^M$ . Given a loss function  $\mathcal{L}$ , the natural procedure to learn the parameters of the regularizer  $R_\theta$  in the denoising problem (4) is to solve

$$\theta_t^*, \lambda_t^* \in \arg \min_{\theta, \lambda} \sum_{m=1}^M \mathcal{L}(\mathbf{T}_{R_\theta, \lambda, \alpha}^t(\mathbf{y}^m), \mathbf{x}^m) \quad (25)$$

for the limiting case  $t = \infty$  and an admissible stepsize  $\alpha$ . Here,  $\mathbf{T}_{R_\theta, \lambda, \alpha}^t$  denotes the  $t$ -fold composition of the gradient-step NN given in (8). In principle, we can optimize the training problem (25) subject to a fixed point condition as in [26], [45], which leads to bi-level optimization. However, it turned out to be unnecessary to fully compute the fixed point  $\mathbf{T}_{R_\theta, \lambda, \alpha}^\infty(\mathbf{y}^m)$  to learn  $R_\theta$  in our constrained setting. Instead, we approximate  $\mathbf{T}_{R_\theta, \lambda, \alpha}^\infty(\mathbf{y}^m)$  using a finite number of steps, which leads to an approximation of the original problem (25). This specifies the  $t$ -step denoiser NN, namely  $\mathbf{T}_{R_\theta, \lambda, \alpha}^t$ , which is trained such that

$$\mathbf{T}_{R_\theta, \lambda, \alpha}^t(\mathbf{y}^m) \simeq \mathbf{x}^m \quad (26)$$

for each  $m = 1, \dots, M$ .

As we show later in Proposition V.1,  $\mathbf{T}_{R_\theta, \lambda, \alpha}^t$  is an averaged mapping. For small  $t$ , this yields a fast-to-evaluate denoiser. Since it is not necessarily a proximal operator, its interpretability is, however, limited.

Once the gradient-step NN is trained, we can plug the corresponding  $R_\theta$  into (4), and fully solve the optimization problem. This yields an interpretable **proximal denoiser**. In practice, turning a  $t$ -step denoiser into a proximal one requires adjusting  $\lambda$  and the addition of a scaling parameter as introduced in Section IV-C. Our numerical experiments in Section VI-A indicate that the number of steps  $t$  used for training the multi-gradient-step denoiser has little influence on the test performances of both the  $t$ -step and proximal denoisers, hence training the model within a few minutes is possible. Note that our method bears some resemblance with the variational networks (VN) proposed in [35], but there are some fundamental differences. While the model used by the authors also involves a sum of convex ridges with learnable profile functions, these are parametrized by RBFs and only the last step of the gradient descent is included in the forward pass. They observed that increasing  $t$  deters the denoising performances which is not the case for our architecture. More implementation differences are outlined in Section IV-B.

##### B. Implementing the Constraints

Our learning of the  $t$ -step denoiser is constrained as follows

- (i) the activation functions  $\sigma_i$  must be increasing (convexity constraint on  $\psi_i$ );
- (ii) the activation functions  $\sigma_i$  must be such that the variational problem (2) has solutions in the generic setting (existence constraint);
- (iii) the stepsize  $\alpha$  in (8) must satisfy the convergence condition, i.e. the gradient-step NN should be an averaged mapping (Lipschitz constraint).

Since the methods to enforce these constraints can have a major impact on the final performance, they must be designed carefully.

a) *Monotonic Splines:* Here, we address constraints (i) and (ii) simultaneously. Similar to [20], [46], we use learnable linear splines  $\sigma_{c^i}: \mathbb{R} \rightarrow \mathbb{R}$  with  $(M+1)$  uniform knots  $\nu_m = (m - M/2)\Delta$ ,  $m = 0, \dots, M$ , where  $\Delta$  is the knot spacing. For simplicity, we assume that  $M$  is even. The learnable parameter  $\mathbf{c}^i = (c_m^i)_{m=0}^M \in \mathbb{R}^{M+1}$  defines the value of  $\sigma_{c^i}$  at the knots, i.e.  $\sigma_{c^i}(\nu_m) = c_m^i$ . To fully characterize  $\sigma_{c^i}$ , we extend it by the constant value  $\mathbf{c}_0^i$  on  $(-\infty, \nu_0]$  and  $\mathbf{c}_M^i$  on  $[\nu_M, +\infty)$ . This choice results in a linear extension for the corresponding indefinite integrals, which show up for the regularizer  $R_\theta$  in (4). Further details on implementing learnable linear splines can be found in [46].

Let  $\mathbf{D} \in \mathbb{R}^{M \times (M+1)}$  be the one-dimensional finite-difference matrix. As  $\sigma_{c^i}$  is piecewise linear, it holds that

$$\sigma_{c^i} \text{ is increasing} \iff \mathbf{D}\mathbf{c}^i \geq 0. \quad (27)$$

In order to optimize over  $\{\sigma_{c^i}: \mathbf{D}\mathbf{c}^i \geq 0\}$ , we reparametrize the linear splines as  $\sigma_{\mathbf{P}_\uparrow(\mathbf{c}^i)}$  where

$$\mathbf{P}_\uparrow = \mathbf{C}\mathbf{D}^\dagger \text{ReLU}(\mathbf{D} \cdot), \quad (28)$$

is a non-linear projection operator onto the feasible set. There,  $\mathbf{D}^\dagger$  denotes the Moore-Penrose inverse of  $\mathbf{D}$  and  $\mathbf{C} = \mathbf{I}_{M+1} - \mathbf{1}_{M+1}\mathbf{e}_{M/2+1}^T$  shifts the output such that the  $(M/2+1)$ th element is zero. In effect, this projection simply preserves the positive finite differences between entries in  $\mathbf{c}^i$  and sets the negative ones to zero. As the associated profile functions  $\psi_i$  are convex and satisfy  $\psi_i'(0) = \sigma_i(0) = 0$ , Proposition III.1 guarantees the existence of a solution for (2).

The proposed change of variable  $\mathbf{c}^i \rightarrow \mathbf{P}_\uparrow(\mathbf{c}^i)$  enables to incorporate the constraint into the forward pass without constraining  $\mathbf{c}_i$  directly. For an efficient forward and backward pass with auto-differentiation,  $\mathbf{P}_\uparrow$  is implemented with the `cumsum` function instead of building the matrix  $\mathbf{D}^\dagger$  explicitly, and the computational overhead is very small. Our approach differs from classical convex optimization—recall that our training problem is nonconvex—where such constraints are instead usually enforced by projecting the coefficients onto the feasible set after each gradient step. The latter method was used for training VNs in [35] with convex  $\psi_i$  parametrized with RBF functions.

b) *Sparse Promoting Regularization:* Using learnable activation functions can lead to over-fitting and weaken the generalizability in the context of non-identity operators  $\mathbf{H}$ . Hence, the training procedure should promote simple linear splines. Here, it is natural to promote the better-performing splines with the fewest knots. This is achieved by penalizing the second-order total variation of each  $\sigma_{c^i}$ , which yields the modified training loss

$$\sum_{m=1}^M \mathcal{L}(\mathbf{T}_{R_\theta, \lambda, \alpha}^t(\mathbf{y}^m), \mathbf{x}^m) + \eta \sum_{i=1}^p \|\mathbf{L}\mathbf{P}_\uparrow(\mathbf{c}_i)\|_1, \quad (29)$$

where  $\mathbf{L} \in \mathbb{R}^{(M-1) \times (M+1)}$  is the second-order finite-difference matrix, and  $\eta \in \mathbb{R}^+$  allows to tune the regularization

strength. We refer the reader to [47] for more theoretical insights into this second-order total-variation regularization and to [46] for experimental evidence of its relevance for machine learning.

c) *Convergent Gradient Steps*: Constraint (iii) guarantees that the  $t$ -fold composition of the gradient-step NN  $T_{R_\theta, \lambda, \alpha}^t$  computes the actual minimizer of (4) for  $t \rightarrow \infty$ . Therefore, it should be enforced in any sensible training method. In addition, it brings stability to the training. To fully exploit the model capacity even for small  $t$ , we need a precise upper bound for  $\text{Lip}(\nabla R_\theta)$ . The estimate that we provide in Proposition IV.1 is an improvement over the classical bound derived from the sub-multiplicativity of the Lipschitz constant for compositional models. It is easily computable as well.

**Proposition IV.1.** *Let  $L_\theta$  denote the Lipschitz constant of  $\nabla R_\theta(\mathbf{x}) = \mathbf{W}^T \boldsymbol{\sigma}(\mathbf{W}\mathbf{x})$  with  $\mathbf{W} \in \mathbb{R}^{p \times d}$  and  $\sigma_i \in C_{\uparrow}^{0,1}(\mathbb{R})$ . Introducing  $\boldsymbol{\Sigma}_\infty = \text{diag}(\|\sigma'_1\|_\infty, \dots, \|\sigma'_p\|_\infty)$ ,  $L_\theta$  satisfies*

$$L_\theta \leq \|\mathbf{W}^T \boldsymbol{\Sigma}_\infty \mathbf{W}\| = \|\sqrt{\boldsymbol{\Sigma}_\infty} \mathbf{W}\|^2, \quad (30)$$

which is tighter than the naive bound

$$L_\theta \leq L_\sigma \|\mathbf{W}\|^2. \quad (31)$$

*Proof.* The bound (31) is a standard result for compositional models. Next, we note that the Hessian of  $R_\theta$  reads

$$\mathbf{H}_{R_\theta}(\mathbf{x}) = \mathbf{W}^T \boldsymbol{\Sigma}(\mathbf{x}) \mathbf{W}, \quad (32)$$

where  $\boldsymbol{\Sigma}(\mathbf{x}) = \text{diag}(\sigma'_1(x_1), \dots, \sigma'_p(x_p))$ . Further, it holds  $L_\theta \leq \sup_{\mathbf{x} \in \mathbb{R}^d} \|\mathbf{H}_{R_\theta}(\mathbf{x})\|$ . Since the functions  $\sigma_i$  are increasing, we have for every  $\mathbf{x} \in \mathbb{R}^p$  that

$$\boldsymbol{\Sigma}_\infty - \boldsymbol{\Sigma}(\mathbf{x}) \succeq 0, \quad (33)$$

and consequently

$$\mathbf{W}^T (\boldsymbol{\Sigma}_\infty - \boldsymbol{\Sigma}(\mathbf{x})) \mathbf{W} \succeq 0. \quad (34)$$

Using the Courant-Fischer theorem, we now infer that the largest eigenvalue of  $\mathbf{W}^T \boldsymbol{\Sigma}_\infty \mathbf{W}$  is greater than that of  $\mathbf{W}^T \boldsymbol{\Sigma}(\mathbf{x}) \mathbf{W}$ .  $\square$

The two bounds meet when the activation functions used are identical, which is typically not the case in our framework. For the 14 NNs trained in Section VI, we found that the improved bound (30) was on average indeed 3.2 times smaller than (31). As the bound (30) depends on the model parameters, it is critical to embed the computation into the forward pass—otherwise, the training gets unstable. This is done by first estimating the normalized eigenvector  $\mathbf{u}$  corresponding to the largest eigenvalue of  $\mathbf{W}^T \boldsymbol{\Sigma}_\infty \mathbf{W}$  via the power iteration method in a non-differentiable way, i.e. under the `torch.no_grad()` context-manager. Then, we directly plug the estimate  $L_\theta \simeq \|\mathbf{W}^T \boldsymbol{\Sigma}_\infty \mathbf{W} \mathbf{u}\|$  in our model and hence embed it in the forward pass. This approach is inspired by the spectral normalization technique proposed in [48], which is a popular and efficient way to enforce Lipschitz constraints on fully connected linear layers. Note that a similar simplification is also proposed and studied in the context of deep equilibrium models [49]. In practice, the estimate  $\mathbf{u}$  is stored so that it can be used as a warm start for the next computation of  $L_\theta$ .

Table I  
PROPERTIES OF DIFFERENT RELIABLE FRAMEWORKS.

	Explicit cost	Convergent	Universal	Shallow	Smooth reg.
TV	✓	✓	✓	✓	✗
ACR	✓	✓	✗	✗	✗
PnP- $\beta$ NN	✗	✓	✓	✗	NA
CRR-NN	✓	✓	✓	✓	✓

### C. Boosting the Universality of the Regularizer

The learnt regularizer  $R_\theta$  depends on the training task (denoising) and noise level. To solve a generic inverse problem, in addition to the regularization strength  $\lambda$ , we propose to incorporate a tunable scaling parameter  $\mu \in \mathbb{R}^+$  and compute

$$\arg \min_{\mathbf{x} \in \mathbb{R}^d} \|\mathbf{H}\mathbf{x} - \mathbf{y}\|_2^2 + \lambda/\mu R_\theta(\mu\mathbf{x}). \quad (35)$$

While the scaling parameter is irrelevant for homogeneous regularizers, such as the Tikhonov and TV ones, it is known to boost the performance within the PnP framework when applied to the input of the denoiser [50].

The cost function in (35) is smooth with Lipschitz continuous gradients, hence the reconstruction is efficiently computed with the accelerated gradient descent. If in addition convex constraints are imposed on  $\mathbf{x}$ , (35) can be computed via the FISTA algorithm [51]. In both cases, the stepsize is set following Corollary IV.2, which provides a precise estimate of the Lipschitz constant of the gradient of the cost function.

**Corollary IV.2.** *The Lipschitz constant  $L_{\text{tot}}$  of the gradient of the objective*

$$x \mapsto \frac{1}{2} \|\mathbf{H}\mathbf{x} - \mathbf{y}\|_2^2 + \lambda/\mu R_\theta(\mu\mathbf{x}) \quad (36)$$

satisfies

$$L_{\text{tot}} \leq \|\mathbf{H}^T \mathbf{H} + \lambda\mu \mathbf{W}^T \boldsymbol{\Sigma}_\infty \mathbf{W}\|, \quad (37)$$

where  $\boldsymbol{\Sigma}_\infty = \text{diag}(\|\sigma'_1\|_\infty, \dots, \|\sigma'_p\|_\infty)$ .

## V. CONNECTIONS TO DEEP LEARNING APPROACHES

Our proposed CRR-NNs have a single non-linear layer, which is rather unusual in the era of deep learning. To further explore their theoretical properties, we briefly discuss two successful deep learning methods, namely the Plug-and-Play (PnP) and Adversarial regularizer (AR) frameworks, and state the most stable and interpretable version that they offer. This will clarify the notions of strict convergence, interpretability, and universality. All comparisons established in this section are synthesized in Table I.

### A. Plug-and-Play and Averaged Denoisers

a) *Convergent Plug-and-Play*: The training procedure proposed for CRR-NNs leads to a convex regularizer  $R_\theta$ , whose proximal operator (4) is a good denoiser. Reciprocally, the proximal operator can be replaced by a powerful denoiser  $D$  in proximal algorithms, which is referred to as PnP. In the

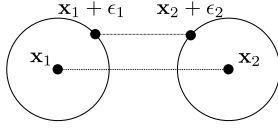


Figure 1. The distance between two noisy images,  $(\mathbf{x}_1 + \epsilon_1)$  and  $(\mathbf{x}_2 + \epsilon_2)$ , can be smaller than that between their clean versions,  $\mathbf{x}_1$  and  $\mathbf{x}_2$ . This limits the performance of a nonexpansive denoiser  $D$  since  $\|D(\mathbf{x}_1 + \epsilon_1) - D(\mathbf{x}_2 + \epsilon_2)\| \leq \|\mathbf{x}_1 + \epsilon_1 - (\mathbf{x}_2 + \epsilon_2)\| < \|\mathbf{x}_1 - \mathbf{x}_2\|$  in the scenario depicted in the figure, and perfect denoising is not possible.

PnP-FBS algorithm derived from (2) [51], [52], the reconstruction is carried out iteratively via

$$\mathbf{x}_{k+1} = D(\mathbf{x}_k - \alpha \mathbf{H}^T(\mathbf{H}\mathbf{x}_k - \mathbf{y})), \quad (38)$$

where  $\alpha$  is the stepsize, and  $D: \mathbb{R}^d \rightarrow \mathbb{R}^d$  is a generic denoiser. A standard set of sufficient conditions<sup>1</sup> to guarantee convergence of the iterations (38) is that

- (i)  $\alpha \in [0, 2/\|\mathbf{H}\|^2]$ ,
- (ii)  $D$  is an averaged operator, namely  $D = \beta N + (1 - \beta)\text{Id}$  where  $\beta \in (0, 1)$  and  $N: \mathbb{R}^n \rightarrow \mathbb{R}^n$  is a nonexpansive mapping, and
- (iii) the set of fixed points for the update operator in (38) is nonempty.

In general, Condition (ii) is not sufficient to ensure that  $D$  is the proximal operator of some convex regularizer  $R$ . Hence, its interpretability is still limited. Further, Condition (i) implies that  $\mathbf{x} \mapsto (\mathbf{x} - \alpha \mathbf{H}^T(\mathbf{H}\mathbf{x} - \mathbf{y}))$  is an averaged operator. Hence, as averagedness is preserved through composition, the iterates are updated by the application of an averaged operator, see [22] for details. Incorporating Condition (iii), the convergence of the iterations (38) now follows from Opial’s convergence theorem.

*b) Constraint Vs Performance:* As already discussed in [17], [33], the performance of the denoiser  $D$  is in direct competition with its averagedness. A simple illustration of this issue is provided in Figure 1. Unsurprisingly, Condition (ii) is not met by any learnt state-of-the-art denoiser, and it is usually also relaxed in the PnP literature.

For instance, it is common to use non 1-Lipschitz learning modules, such as batch normalization [19], or to only constrain the residual  $(\text{Id} - D)$  to be nonexpansive, which enables to train a nonexpansive NN in a residual way [19], [22], [53]. Another recent approach consists in penalizing in the training loss either the norm of the Jacobian of  $D$  at a finite set of locations [33], [37] or of another local estimate of the Lipschitz constant [54]. Interestingly, even slightly relaxed frameworks usually yield significant reconstruction quality improvements. However, they do not provide convergence guarantees for ill-posed inverse problems, which is problematic for sensitive applications such as biomedical imaging.

*c) Averaged Deep NNs and CRR-NNs:* To leverage the success of deep learning, the mapping  $N$  is typically chosen as a deep CNN of the form<sup>2</sup>

$$N = C_K \circ \sigma \circ \dots \circ C_2 \circ \sigma \circ C_1, \quad (39)$$

where  $C_k$  are learnable convolutional layers, and  $\sigma$  is the activation function [19], [20], [48]. To meet Condition (ii),  $N$  must be nonexpansive, which is usually achieved by constraining  $C_k$  and  $\sigma$  to be nonexpansive. This is predicated on the fact that the Lipschitz constant is sub-multiplicative with respect to the composition operation. Intuitively, this approach leads to looser Lipschitz bounds for deeper models. As a matter of fact, the benefit of depth is unclear: the gain of expressivity usually brought by extra layers is reduced by the Lipschitz bound which becomes more pessimistic, i.e. it overestimates the Lipschitz constant even more. Put differently, these CNNs can easily learn the zero function while they struggle to generate less contractive mappings with a Lipschitz constant of one for instance. For the same reason, the learning process is also prone to vanishing gradients in this constrained setting.

Under Lipschitz constraints, the zero-gradient region of the popular ReLU activation function causes provable limitations [55]–[57]. Some of these can be resolved by using PReLU activation functions instead. In the sequel, we denote the PnP method with an averaged CNN and PReLU activation functions by PnP- $\beta$ NN. Interestingly, the model  $\mathbf{T}_{R_\theta, \lambda, \alpha}$  given in (8) also offers a parametrization of averaged mappings.

**Proposition V.1.** *Let  $L_\theta$  be the Lipschitz constant of  $\nabla R_\theta$  given in (7). For  $\alpha \in (0, 2/(1 + \lambda L_\theta))$ , the gradient-step NN  $\mathbf{T}_{R_\theta, \lambda, \alpha}$  given in (8) is  $(\alpha(1 + \lambda L_\theta)/2)$ -averaged.*

*Proof.* Since  $\mathbf{T}_{R_\theta, \lambda, \alpha}$  is the gradient-step of a convex function, we can apply the same reasoning as in the proof of [22, Proposition 15].  $\square$

The structure of  $\mathbf{T}_{R_\theta, \lambda, \alpha}$  is radically different from standard deep averaged CNNs as in (39). We believe that this is key to account for the observed improvements. The operator  $\mathbf{T}_{R_\theta, \lambda, \alpha}$  (and by consequence  $\mathbf{T}_{R_\theta, \lambda, \alpha}^\infty$ ) can easily generate the identity mapping (all weights are 0 and  $\alpha = 1$ ), which appears as a natural requirement for a good and easy to train denoiser. This intuition is supported by our experiments in Section VI, in which we found that CRR-NNs’  $t$ -step and proximal denoisers both outperform averaged deep NNs, while their training times are two orders of magnitude smaller.

## B. Adversarial Regularizers

Contrary to PnP methods, the Adversarial Regularizer (AR) framework [28] allows to directly learn a (possibly non-convex) regularizer  $R$ , resulting in an interpretable energy functional. The regularizer is learnt by minimizing its value on clean images, and maximizing its value on unregularized reconstructions<sup>3</sup>. In this way, the learnt regularizer can be non-smooth and there is no need for heavy learning procedures such as bi-level optimization. To obtain the unregularized reconstructions, the operator  $\mathbf{H}$  has to be known before training the model. This is a key difference with CRR-NNs and PnP methods, where the training is independent of  $\mathbf{H}$  (universality property). If  $R$  is non-convex, the initialization and the actually chosen minimization method for solving

<sup>1</sup>Here,  $\mathbf{H}$  can be non-invertible, otherwise weaker conditions exist [19].

<sup>2</sup>The benefit of adding skip connections for nonexpansive NNs is unclear.

<sup>3</sup>To ensure stable training, an estimate of the Lipschitz constant of the network is penalized to prevent large gradients.

the inverse problem (2) become important. The Adversarial Convex Regularizer (ACR) framework [38], [39] was proposed to circumvent such considerations and increase the reliability of the method. Here, the architecture of the regularizer is a deep Input Convex NN (ICNN) [40] with leaky-ReLU activation function (typically 10 layers and around 500 000 parameters). The regularizer is convex but non-smooth—a potential drawback for optimization techniques, but the authors in [38] did not find any practical issues in that matter. To boost the performance of the regularizer, the authors added a so-called sparsifying filter bank (SFB) to the ICNN, namely a convex term of the form  $\|\mathbf{U}\mathbf{x}\|_1$ , where the linear operator  $\mathbf{U}$  is made of convolutions learnt jointly with the ICNN.

## VI. EXPERIMENTS

### A. Training CRR-NNs

The CRR-NNs are trained on a Gaussian denoising task with noise levels  $\sigma \in \{5/255, 25/255\}$ . The same procedure as in [19], [58] is used to form 238,400 patches of size  $(40 \times 40)$  from 400 images of the BSD500 dataset [59]. For validation, the same 12 images as in [19], [58] are used. The weights  $\mathbf{W}$  in  $R_\theta$  are parametrized as the composition of two zero-padded convolutions with kernels of size  $(7 \times 7)$  and with 8 and 32 output channels, respectively. This composition of two linear components, although not more expressive theoretically, facilitates the patch-based training of CRR-NNs. For inference, the convolutional layer can then be transformed back to a single convolution. Similar to [26], the kernels of the convolutions are constrained to have zero mean. Lastly, the linear splines have  $(M + 1) = 21$  equally distant knots with  $\Delta = 0.01$ , and the sparsifying regularization parameter is  $\eta = 5 \cdot 10^{-3}\sigma$ . We initially set  $\mathbf{c}_i = \mathbf{0}$ .

The CRR-NNs are trained for 10 epochs with  $t \in \{1, 2, 5, 10, 20, 30, 50\}$  gradient steps. For this purpose, the  $\ell_1$  loss is used along with the Adam optimizer with its default parameters  $(\beta_1, \beta_2) = (0.9, 0.999)$ , and the batch size is set to 128. Further, the learning rates are decayed with rate 0.75 at each epoch and initially set to 0.05 for the parameters  $\lambda$  and  $\mu$ , to  $10^{-3}$  for  $\mathbf{W}$ , and to  $5 \cdot 10^{-5}$  for the  $\mathbf{c}_i$ .

For a given  $t$ , the training yields two averaged denoisers:

- **$t$ -step denoiser:** This corresponds to  $\mathbf{T}_{R_\theta, \lambda, \alpha}^t$  and is the denoiser optimized during training. It should be compared to properly constrained PnP methods based on averaged deep denoisers as in [20], [36], which in general also do not correspond to minimizing an energy.
- **proximal denoiser:** The learnt regularizer  $R_\theta$  is plugged into (35) with  $\mathbf{H} = \mathbf{I}$ , and the solution computed with the accelerated gradient descent with high precision for convergence ( $10^{-6}$  for the relative change of norm between consecutive iterates). The parameters  $\lambda$  and  $\mu$  are tuned on the validation dataset with the coarse-to-fine method given in Appendix A. This important step enables to compensate for the gap between (1) gradient-step training and full minimization, and (2) training and testing noise levels, if different.

Table II  
DENOISING PERFORMANCE OF AVERAGED DENOISERS ON THE BSD68 DATASET

	averaged*	proximal*	$\sigma = 5$	$\sigma = 25$
TV [60]	✓	✓	36.41	27.48
Higher-order MRFs [26]	✓	✓	NA	28.04
$\text{VN}^{1,t**}$ [35]	?	?	NA	27.69
$\text{DnCNN}_\sigma^{0.5}$	✓	?	36.48	27.69
$\text{D}_{\text{ISTA}}$ [36]	✓	?	36.54	NA
$\text{D}_{\text{ADMM}}$ [36]	✓	?	36.62	NA
CRR-NN ( $t$ -step)**	✓	?	<b>36.97</b>	<b>28.12</b>
CRR-NN (proximal)	✓	✓	<b>36.96</b>	<b>28.11</b>

\* We use ? when the property is not guaranteed in general.

\*\* We report the best result over  $t$ .

### B. Denoising Results

Although not the final goal, image denoising yields valuable insights into the training of CRR-NNs. It also enables us to compare CRR-NNs to the related methods given in Table II on the standard BSD68 test set.

We now briefly give the implementation details of the various frameworks. To get an averaged deep CNN denoiser,  $\text{DnCNN}_\sigma^{0.5} = 0.5(N + \text{Id})$  is trained on the same denoising task as the CRR-NNs with  $\sigma \in \{5/255, 25/255\}$ . Here,  $N$  is chosen as a DnCNN [58] with 9 layers, 64 channels, and PReLU activation functions, resulting in 260 225 learnable parameters. The model is trained for 20 epochs with a batch size of 4 and a learning rate of  $4 \cdot 10^{-5}$ . To guarantee that  $N$  is nonexpansive, the linear layers are spectral-normalized after each gradient step with the real-SN method [19], and the activations are constrained to be 1-Lipschitz. This CNN outperforms the averaged CNNs in [20]. Hence, it serves as a baseline for averaged deep CNNs. The other related frameworks do not provide public implementations. Therefore, the numbers are simply taken from the corresponding papers. Lastly, the TV denoising is performed with the algorithm proposed in [60]. The results in Table II and Figure 2 suggest the following:

- **$t$ -step/averaged denoisers:** The CRR-NN implementation improves over the special instance  $\text{VN}^{1,t}$  of variational network denoisers proposed in [35], which also correspond to a partial minimization of a convex cost. With a convex model similar to CRR-NNs, see Section IV for a discussion, it is shown that increasing  $t$  decreases the performance (reported as  $\text{VN}_{24}^{1,t}$  in [35, Figure 5]). The model  $\text{VN}^{1,t}$  cannot compete with the proximal denoiser trained with bi-level optimization in [26]. By contrast, we obtain for  $\sigma = 25$  an improvement over  $\text{VN}^{1,t}$  of 0.2dB for  $t = 1$ , and more than 0.6dB as  $t$  increases. Note that in [35] the  $t$ -step  $\text{VN}^{1,t}$  denoiser is not guaranteed to be averaged. Our models also outperform the averaged  $\text{DnCNN}_\sigma^{0.5}$  (+0.5dB for  $\sigma = 5$ , +0.4dB for  $\sigma = 25$ ), and the two averaged denoisers  $\text{D}_{\text{ISTA}}$  and  $\text{D}_{\text{ADMM}}$  [36] (+0.4/+0.3dB for  $\sigma = 5$ ). In their simplest forms, the latter are built with fixed linear layers (patch-based wavelet transforms) and learnable soft-thresholding activation functions.

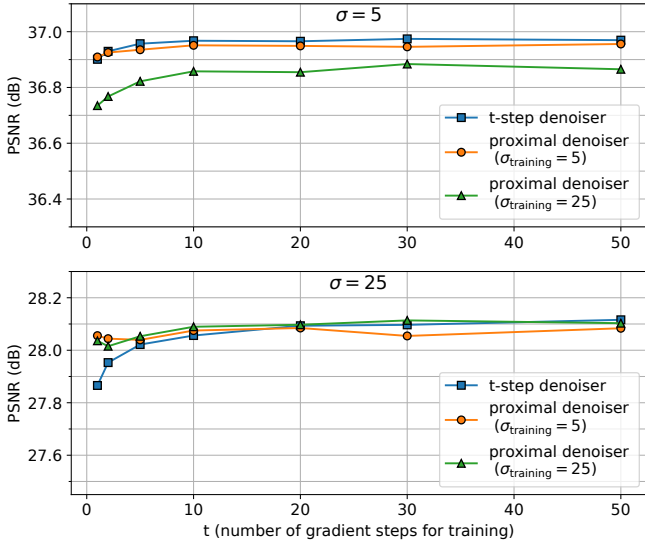


Figure 2. Test denoising performances of CRR-NNs for noise level  $\sigma = 5$  and  $\sigma = 25$  depending on the number of gradient steps used for training, the denoiser type ( $t$ -step vs proximal) and the noise level used for training.

- **proximal denoisers:** Our models yield slight improvements over the higher-order MRF model presented in the pioneering work [26] (28.04dB vs 28.11dB for  $\sigma = 25$ ). With a similar architecture—but with fixed smoothed absolute value  $\psi_i$ —the latter approach relies on a computationally intensive training involving bi-level optimization with second-order solvers. Here, we show that a few gradient steps  $t$  for training already suffice to be competitive. This leads to ultra-fast training and bridges the gap between higher-order MRF models and VN denoisers. Lastly, we remark that the training noise level has only a minor impact when testing a tuned proximal denoiser for a different noise level.

### C. Application to Biomedical Image Reconstruction

The six CRR-NNs trained on denoising with  $t \in \{1, 10, 50\}$  and  $\sigma \in \{5, 25\}$  are now used to solve the following two ill-posed inverse problems.

*a) MRI:* The ground truth is chosen to be fully sampled knee MR images with size  $(320 \times 320)$  from the fastMRI dataset [61]. The validation and test sets consist of 10 and 99 images individually normalized within the range  $[0, 1]$ . The corresponding Fourier measurements are subsampled via a Cartesian mask that is specified by two parameters: the acceleration  $M_{\text{acc}} = 4$  and the center fraction  $M_{\text{cf}} = 0.08$ . All the  $\lfloor 320M_{\text{cf}} \rfloor$  columns in the center of the k-space (low frequencies) are kept, while columns in the other region of the k-space are uniformly sampled so that the total number of selected columns is  $\lfloor 320/M_{\text{acc}} \rfloor$ . Lastly, Gaussian noise with standard deviation  $\sigma_{\text{n}} = 10^{-4}$  is added to the real and imaginary parts of the measurements.

*b) Sparse-view CT:* To provide a fair comparison with the ACR method, we now target the sparse-view CT experiment proposed in [38]. The data consists of human abdominal

Table III  
PSNR AND SSIM VALUES FOR THE MRI RECONSTRUCTION EXPERIMENT.

Metric	$(M_{\text{acc}}, M_{\text{cf}})$ (4, 0.08)	
	PSNR	SSIM
Zero-fill	27.92	0.7105
TV	32.03	0.7922
PnP- $\beta$ NN	31.42	0.8053
CRR-NN ( $\sigma = 5, t = 1$ )	32.88	0.8332
CRR-NN ( $\sigma = 5, t = 10$ )	32.82	0.8314
CRR-NN ( $\sigma = 5, t = 50$ )	32.83	0.8314
CRR-NN ( $\sigma = 25, t = 1$ )	33.12	0.8421
CRR-NN ( $\sigma = 25, t = 10$ )	<b>33.14</b>	<b>0.8415</b>
CRR-NN ( $\sigma = 25, t = 50$ )	33.07	0.8391

Table IV  
PSNR AND SSIM VALUES FOR THE CT RECONSTRUCTION EXPERIMENT.

Metric	PSNR	SSIM
FBP	21.29	0.204
TV	31.57	0.852
PnP- $\beta$ NN	30.82	0.786
ACR [38], [39]	31.58	0.848
CRR-NN ( $\sigma = 5, t = 1$ )	32.58	0.856
CRR-NN ( $\sigma = 5, t = 10$ )	32.63	0.852
CRR-NN ( $\sigma = 5, t = 50$ )	32.59	0.855
CRR-NN ( $\sigma = 25, t = 1$ )	<b>32.87</b>	0.862
CRR-NN ( $\sigma = 25, t = 10$ )	32.79	<b>0.864</b>
CRR-NN ( $\sigma = 25, t = 50$ )	32.79	0.861

CT scans for 10 patients provided by Mayo Clinic for the low-dose CT grand challenge [62]. The validation set consists of 6 images taken uniformly from the first patient of the training set from [38]. We use the same test set as [38], namely 128 slices with size  $(512 \times 512)$  corresponding to one patient. The projections of the data are simulated using a parallel-beam acquisition geometry with 200 angles and 400 detectors. Lastly, Gaussian noise with standard deviation  $\sigma_{\text{n}} = 2.0$  is added to the measurements.

*c) Reconstruction Frameworks:* The reconstructions are computed from the variational formulation (35) via the FISTA algorithm [51] for CRR-NNs and TV regularization. This algorithm allows to easily apply a positivity constraint on the reconstruction. The proximal operator in the FISTA scheme is the projection onto the set of positive-valued images for CRR-NNs, and it is computed as in [63] for the isotropic TV regularizer. We also consider reconstructions obtained using the FBS-PnP method with the averaged denoisers  $\text{DnCNN}_{5/255}^{0.5}$  and  $\text{DnCNN}_{25/255}^{0.5}$ . To adapt these denoisers to different noise levels, we replace them with relaxed versions  $D_{\gamma} = \gamma \text{DnCNN}_{\sigma}^{0.5} + (1 - \gamma)I$ , where  $\gamma \in (0, 1]$  is a tunable hyperparameter that remains fixed throughout the FBS iterations. We only report the best-performing model among the two denoisers. The hyperparameters for all these methods are tuned to maximize the average PSNR over the validation set with the coarse-to-fine method given in Appendix A. The ACR framework [38] yields a convex regularizer for (2) that is specifically designed for the described CT problem. To be consistent with [38], [39], we use the hyperparameters given in their paper and code, both for training and for solving the inverse problem. For the latter, it includes  $\lambda$  and for the

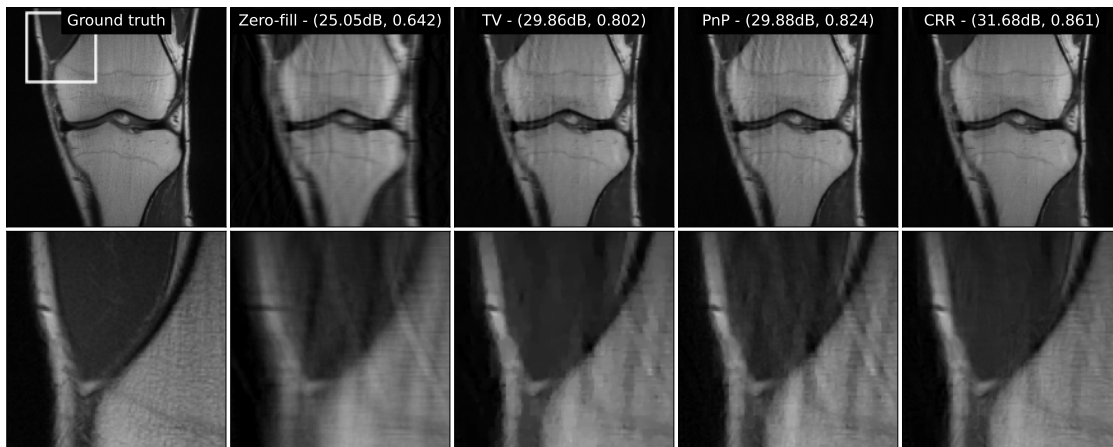


Figure 3. Reconstructed images for the MRI experiment. The metrics reported are the PSNR and SSIM.

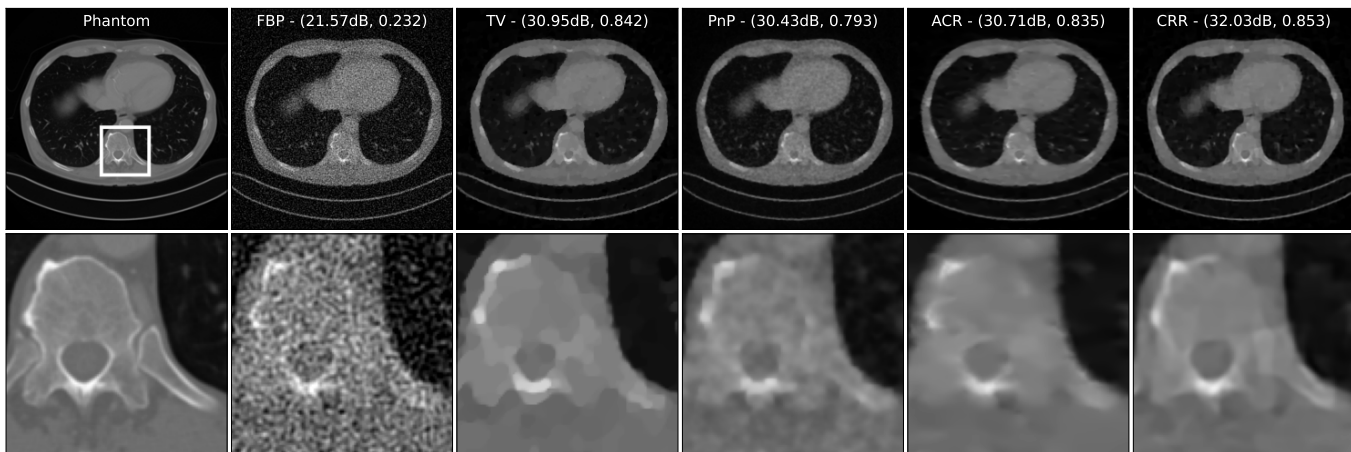


Figure 4. Reconstructed images for the sparse view CT experiment. The metrics reported are the PSNR and SSIM.

gradient descent algorithm the stepsize and the number of iterations. The tuning of the latter two is specific to ACRs since the regularizer is non-smooth, and performing a full minimization with a gradient descent is not obvious.

*d) Results and Discussion:* The PSNR and SSIM values for the test set given in Tables III and IV show that CRR-NNs consistently outperform the other frameworks regardless of the parameters  $(\sigma, t)$  used for training. For each modality, a reconstruction example is given for each framework in Figures 3 and 4. Note that contrary to the denoising experiment, the PnP- $\beta$ NN is now hardly competing with TV. This is potentially due to the difference between the training (denoising) and testing (MRI/CT) tasks. For the CRR-NNs, the noise level used during training now has some minor influence on the results. As there is no clear correlation between performance and the number of gradient steps  $t$ , we recommend using  $t \leq 5$  in practice for an ultra-fast training. Overall, the results illustrate the universality and efficiency of our proposed method.

#### D. Under the Hood of the Learnt Regularizers

The filters and activation functions learnt for our CRR-NNs with  $\sigma \in \{5, 25\}$  and  $t = 5$  are shown in Figures 5 and 6.

*1) Filters:* The impulse responses of the filters have various orientations and differ by their frequency response. This indicates that the CRR-NN decouples the frequency components of patches. The learnt kernels typically come in groups that are reminiscent of 2D steerable filters [64], [65]. Interestingly, their support is greater when the denoising task is carried out for  $\sigma = 25$  compared to  $\sigma = 5$ .

*2) Activation Functions:* The linear splines converge to simple functions throughout the training. Adding the regularization (29) leads to even simpler ones without compromising performance. Most of them end up with 3 linear regions, with their shape being reminiscent of the clipping function  $\text{Clip}(x) = \text{sign}(x) \min(|x|, 1)$ . The learnt regularizer is closely related to  $\ell_1$ -norm based regularization as many of the learnt convex profile functions  $\psi_i$  resemble some smoothed version of the absolute value function. Since the NN has a simple architecture, it can be efficiently pruned before inference by removing the filters associated with almost vanishing activation functions. This yields models with typically no more than 3000 parameters. This offers a clear advantage over deep models, which can usually not be pruned efficiently.

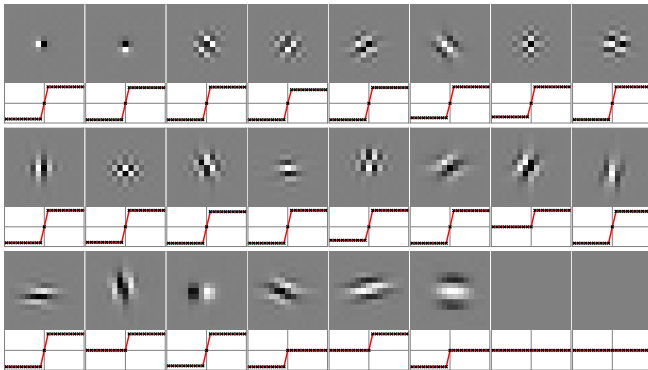


Figure 5. Impulse responses of the filters and activation functions of the CRR-NN trained with  $\sigma = 5$ . The black crosses indicate the knots of the splines. For the 8 missing filters, the associated activation functions were numerically identical to zero.

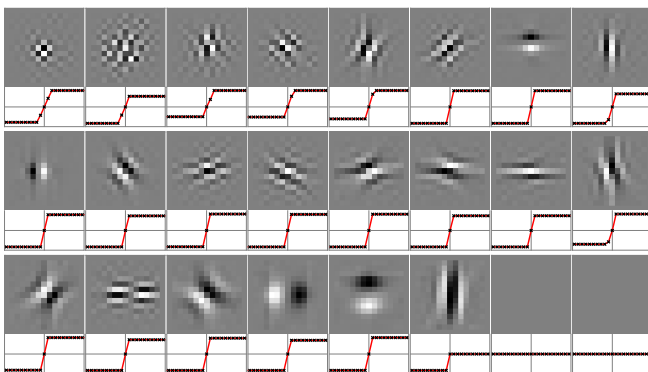


Figure 6. Impulse responses of the filters and activation functions of the CRR-NN trained with  $\sigma = 25$ .

3) *A Signal Processing Interpretation:* Given that the gradient-step operator  $\mathbf{x} \mapsto \mathbf{x} - \alpha \mathbf{W}^T \sigma(\mathbf{W}\mathbf{x})$  of the learnt regularizer is expected to remove some noise from  $\mathbf{x}$ , the 1-hidden-layer CNN  $\mathbf{W}^T \sigma(\mathbf{W}\cdot)$  is expected to extract noise. The response of  $\mathbf{x}$  to the learnt filters forms the high dimensional representation  $\mathbf{W}\mathbf{x}$  of  $\mathbf{x}$ . The clipping function maintains the small responses to the filters, while it cuts the large ones. Hence, the estimated noise  $\mathbf{W}^T \sigma(\mathbf{W}\mathbf{x})$  is reconstructed by essentially removing the components of  $\mathbf{x}$  that have a significant correlation with the kernels of the filters. All in all, learning activation functions leads closely to wavelet- or framelet-like denoising. Indeed, the proximal operator of  $\mathbf{x} \mapsto \|\text{DWT}(\mathbf{x})\|_1$  is given by

$$\text{prox}_{\|\text{DWT}(\cdot)\|_1}(\mathbf{x}) = \text{IDWT}(\text{soft}(\text{DWT}(\mathbf{x}))) \quad (40)$$

$$= \mathbf{x} - \text{IDWT}(\text{clip}(\text{DWT}(\mathbf{x}))), \quad (41)$$

where  $\text{soft}(\cdot)$  is the soft-thresholding function, DWT and IDWT are the orthogonal discrete wavelet transform and its inverse. The equivalent formulation with the clipping function follows from  $\text{IDWT}(\text{DWT}(\mathbf{x})) = \mathbf{x}$  and  $\text{soft}(\mathbf{x}) = \mathbf{x} - \text{clip}(\mathbf{x})$ . The soft-thresholding function is used for direct denoising while the clipping function is tailored to residual denoising. Note that the given analogy is, however, limited since the learnt filters are not orthonormal ( $\mathbf{W}^T \mathbf{W} \neq \mathbf{I}$ ).

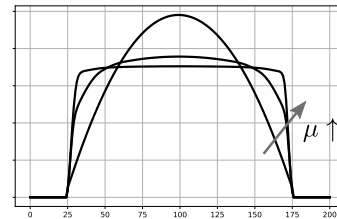


Figure 7. Solutions of the one-dimensional problem (42) for increasing values of  $\mu$ . The plotted functions are supported in  $[25, 175]$  and minimize the learnt regularizer given a unit sum of their values.

4) *Role of the Scaling Factor:* To clarify the role of the scaling factor  $\mu$  introduced in (35), we investigate a toy problem on the space of one-dimensional signals. Since these can be interpreted as images varying along a single direction, a signal regularizer  $R_1$  can be obtained from  $R_\theta$  by replacing the 2D convolutional filters with 1D convolutional filters whose kernels are the ones of  $R_\theta$  summed along a direction. Next, we seek a compactly supported signal with fixed mass that has minimum regularization cost, namely

$$\hat{\mathbf{c}} = \arg \min_{\mathbf{c} \in \mathbb{R}^d} R_1(\mu \mathbf{c}) \quad \text{s.t.} \quad \begin{cases} \mathbf{1}^T \mathbf{c} = 1, \\ \mathbf{c}_k = 0, \quad \forall k \notin [k_1, k_2]. \end{cases} \quad (42)$$

The solutions for various values of  $\mu$  are shown in Figure 7. Small values of  $\mu$  promote smooth functions in a way similar to the Tikhonov regularizer applied to the finite differences. Large values of  $\mu$  promote functions with constant portions and conjointly allows for sharp jumps, which is reminiscent of the TV regularizer. This reasoning is in agreement with the final shape of the activation functions, see Figure 5 and 6. Indeed, increasing  $\mu$  allows enlarging the region where the regularizer has constant gradients while decreasing  $\mu$  allows enlarging the region where the regularizer has linear gradients.

## VII. CONCLUSION

In this work, we have proposed a framework to learn universal convex-ridge regularizers with adaptive profile functions. Our framework is competitive for solving inverse problems over recent deep-learning approaches that also prioritize the reliability of the method. Not only it is faster to train, but it also offers significant improvements in image quality. The findings raise the question of whether shallow models such as CRR-NNs, despite their few number of parameters, already offer optimal performances among methods that rely either on a learnable convex regularizer or on the PnP framework with an averaged denoiser.

## ACKNOWLEDGMENT

The research leading to these results was supported by the European Research Council (ERC) under European Union's Horizon 2020 (H2020), Grant Agreement - Project No 101020573 FunLearn and by the Swiss National Science Foundation, Grant 200020 184646/1. The authors are thankful to Dimitris Perdios for helpful discussions.

## REFERENCES

- [1] A. Ribes and F. Schmitt, "Linear inverse problems in imaging," *IEEE Signal Processing Magazine*, vol. 25, no. 4, pp. 84–99, 2008.
- [2] M. T. McCann and M. Unser, "Biomedical image reconstruction: From the foundations to deep neural networks," *Foundations and Trends® in Signal Processing*, vol. 13, no. 3, pp. 283–359, 2019.
- [3] A. N. Tikhonov, "Solution of incorrectly formulated problems and the regularization method," *Soviet Mathematics*, vol. 4, pp. 1035–1038, 1963.
- [4] L. I. Rudin, S. Osher, and E. Fatemi, "Nonlinear total variation based noise removal algorithms," *Physica D: nonlinear phenomena*, vol. 60, no. 1-4, pp. 259–268, 1992.
- [5] D. L. Donoho, "Compressed sensing," *IEEE Transactions on information theory*, vol. 52, no. 4, pp. 1289–1306, 2006.
- [6] E. J. Candès and M. B. Wakin, "An introduction to compressive sampling," *IEEE signal processing magazine*, vol. 25, no. 2, pp. 21–30, 2008.
- [7] S. Arridge, P. Maass, O. Öktem, and C.-B. Schönlieb, "Solving inverse problems using data-driven models," *Acta Numer.*, vol. 28, pp. 1–174, 2019.
- [8] G. Ongi, A. Jalal, C. A. Metzler, R. G. Baraniuk, A. G. Dimakis, and R. Willett, "Deep learning techniques for inverse problems in imaging," *IEEE Journal on Selected Areas in Information Theory*, vol. 1, no. 1, pp. 39–56, 2020.
- [9] V. Antun, F. Renna, C. Poon, B. Adcock, and A. C. Hansen, "On instabilities of deep learning in image reconstruction and the potential costs of ai," *Proceedings of the National Academy of Sciences*, vol. 117, no. 48, pp. 30088–30095, 2020.
- [10] N. M. Gottschling, V. Antun, B. Adcock, and A. C. Hansen, "The troublesome kernel: why deep learning for inverse problems is typically unstable," *arXiv:2001.01258*, 2020.
- [11] K. H. Jin, M. T. McCann, E. Froustey, and M. Unser, "Deep convolutional neural network for inverse problems in imaging," *IEEE Transactions on Image Processing*, vol. 26, no. 9, pp. 4509–4522, 2017.
- [12] H. Chen, Y. Zhang, W. Zhang, P. Liao, K. Li, J. Zhou, and G. Wang, "Low-dose CT via convolutional neural network," *Biomedical Optics Express*, vol. 8, no. 2, pp. 679–694, Feb 2017.
- [13] B. Zhu, J. Z. Liu, S. F. Cauley, B. R. Rosen, and M. S. Rosen, "Image reconstruction by domain-transform manifold learning," *Nature*, vol. 555, no. 7697, pp. 487–492, 2018.
- [14] C. M. Hyun, H. P. Kim, S. M. Lee, S. Lee, and J. K. Seo, "Deep learning for undersampled MRI reconstruction," *Physics in Medicine & Biology*, vol. 63, no. 13, p. 135007, 2018.
- [15] P. Hagemann and S. Neumayer, "Stabilizing invertible neural networks using mixture models," *Inverse Problems*, vol. 37, no. 8, p. 085002, 2021.
- [16] S. V. Venkatakrishnan, C. A. Bouman, and B. Wohlberg, "Plug-and-play priors for model based reconstruction," in *IEEE Global Conference on Signal and Information Processing*, 2013, pp. 945–948.
- [17] S. H. Chan, X. Wang, and O. A. Elgandy, "Plug-and-play ADMM for image restoration: Fixed-point convergence and applications," *IEEE Transactions on Computational Imaging*, vol. 3, no. 1, pp. 84–98, 2016.
- [18] Y. Romano, M. Elad, and P. Milanfar, "The little engine that could: Regularization by denoising (RED)," *SIAM Journal on Imaging Sciences*, vol. 10, no. 4, pp. 1804–1844, 2017.
- [19] E. Ryu, J. Liu, S. Wang, X. Chen, Z. Wang, and W. Yin, "Plug-and-play methods provably converge with properly trained denoisers," in *Proceedings of the 36th International Conference on Machine Learning*, ser. Proceedings of Machine Learning Research, vol. 97. PMLR, 09–15 Jun 2019, pp. 5546–5557.
- [20] P. Bohra, D. Perdios, A. Goujon, S. Emery, and M. Unser, "Learning Lipschitz-controlled activation functions in neural networks for Plug-and-Play image reconstruction methods," in *NeurIPS 2021 Workshop on Deep Learning and Inverse Problems*, 2021.
- [21] M. Hasannasab, J. Hertrich, S. Neumayer, G. Plonka, S. Setzer, and G. Steidl, "Parseval proximal neural networks," *The Journal of Fourier Analysis*, vol. 26, p. 59, 2020.
- [22] J. Hertrich, S. Neumayer, and G. Steidl, "Convolutional proximal neural networks and Plug-and-Play algorithms," *Linear Algebra Appl.*, vol. 631, pp. 203–234, 2021.
- [23] H. Gupta, K. H. Jin, H. Q. Nguyen, M. T. McCann, and M. Unser, "CNN-based projected gradient descent for consistent CT image reconstruction," *IEEE transactions on medical imaging*, vol. 37, no. 6, pp. 1440–1453, 2018.
- [24] S. Hurault, A. Leclaire, and N. Papadakis, "Gradient step denoiser for convergent Plug-and-Play," in *International Conference on Learning Representations*, 2022.
- [25] S. Roth and M. J. Black, "Fields of experts," *International Journal of Computer Vision*, vol. 82, no. 2, pp. 205–229, 2009.
- [26] Y. Chen, R. Ranftl, and T. Pock, "Insights into analysis operator learning: From patch-based sparse models to higher order MRFs," *IEEE transactions on image processing*, vol. 23, pp. 1060–72, 2014.
- [27] A. Effland, E. Kobler, K. Kunisch, and T. Pock, "Variational networks: An optimal control approach to early stopping variational methods for image restoration," *Journal of mathematical imaging and vision*, vol. 62, no. 3, pp. 396–416, 2020.
- [28] S. Lunz, O. Öktem, and C.-B. Schönlieb, "Adversarial regularizers in inverse problems," *Advances in neural information processing systems*, vol. 31, 2018.
- [29] M. Duff, N. D. F. Campbell, and M. J. Ehrhardt, "Regularising inverse problems with generative machine learning models," *arXiv:2107.11191*, 2021.
- [30] H. Li, J. Schwab, S. Antholzer, and M. Haltmeier, "NETT: solving inverse problems with deep neural networks," *Inverse Problems*, vol. 36, no. 6, p. 065005, 2020.
- [31] E. Kobler, A. Effland, K. Kunisch, and T. Pock, "Total deep variation for linear inverse problems," in *IEEE/CVF Conference on Computer Vision and Pattern Recognition (CVPR)*, June 2020.
- [32] R. Cohen, Y. Blau, D. Freedman, and E. Rivlin, "It has potential: Gradient-driven denoisers for convergent solutions to inverse problems," *Advances in Neural Information Processing Systems*, vol. 34, 2021.
- [33] S. Hurault, A. Leclaire, and N. Papadakis, "Proximal denoiser for convergent Plug-and-Play optimization with nonconvex regularization," in *Proceedings of the 39th International Conference on Machine Learning*, ser. Proceedings of Machine Learning Research, vol. 162. PMLR, 17–23 Jul 2022, pp. 9483–9505.
- [34] R. Fermanian, M. L. Pendu, and C. Guillemot, "Learned gradient of a regularizer for Plug-and-Play gradient descent," *arXiv:2204.13940*, 2022.
- [35] E. Kobler, T. Klatzer, K. Hammernik, and T. Pock, "Variational networks: Connecting variational methods and deep learning," in *Pattern Recognition*, 2017, pp. 281–293.
- [36] P. Nair and K. N. Chaudhury, "On the construction of averaged deep denoisers for image regularization," *arXiv:2207.07321*, 2022.
- [37] J.-C. Pesquet, A. Repetti, M. Terris, and Y. Wiaux, "Learning maximally monotone operators for image recovery," *SIAM Journal on Imaging Sciences*, vol. 14, no. 3, pp. 1206–1237, 2021.
- [38] S. Mukherjee, S. Dittmer, Z. Shumaylov, S. Lunz, O. Öktem, and C.-B. Schönlieb, "Learned convex regularizers for inverse problems," *arXiv:2008.02839*, 2021.
- [39] S. Mukherjee, C.-B. Schönlieb, and M. Burger, "Learning convex regularizers satisfying the variational source condition for inverse problems," in *NeurIPS Workshop on Deep Learning and Inverse Problems*, 2021.
- [40] B. Amos, L. Xu, and J. Z. Kolter, "Input convex neural networks," in *Proceedings of the 34th International Conference on Machine Learning*, ser. Proceedings of Machine Learning Research, vol. 70. PMLR, 06–11 Aug 2017, pp. 146–155.
- [41] H. Q. Nguyen, E. Bostan, and M. Unser, "Learning convex regularizers for optimal bayesian denoising," *IEEE Transactions on Signal Processing*, vol. 66, no. 4, pp. 1093–1105, 2017.
- [42] G. Peyré and J. M. Fadili, "Learning analysis sparsity priors," in *SampTA'11*, 2011, pp. 4–pp.
- [43] Y. Chen, T. Pock, and H. Bischof, "Learning 11-based analysis and synthesis sparsity priors using bi-level optimization," in *26th Neural Information Processing Systems Conference*, 2012.
- [44] L. B. Willner, "On the distance between polytopes," *Quarterly of Applied Mathematics*, vol. 26, no. 2, pp. 207–212, 1968.
- [45] S. Bai, J. Z. Kolter, and V. Koltun, "Deep equilibrium models," in *Advances in Neural Information Processing Systems*, vol. 32, 2019.
- [46] P. Bohra, J. Campos, H. Gupta, S. Aziznejad, and M. Unser, "Learning activation functions in deep (spline) neural networks," *IEEE Open Journal of Signal Processing*, vol. 1, pp. 295–309, 2020.
- [47] M. Unser, "A representer theorem for deep neural networks," *Journal of Machine Learning Research*, vol. 20, no. 110, pp. 1–30, 2019.
- [48] T. Miyato, T. Kataoka, M. Koyama, and Y. Yoshida, "Spectral normalization for generative adversarial networks," in *International Conference on Learning Representations*, 2018.
- [49] S. W. Fung, H. Heaton, Q. Li, D. McKenzie, S. Osher, and W. Yin, "JFB: Jacobian-free backpropagation for implicit networks," in *Proceedings of the AAAI Conference on Artificial Intelligence*, 2022.

- [50] X. Xu, J. Liu, Y. Sun, B. Wohlberg, and U. S. Kamilov, “Boosting the performance of Plug-and-Play priors via denoiser scaling,” in *54th Asilomar Conference on Signals, Systems, and Computers*, 2020, pp. 1305–1312.
- [51] A. Beck and M. Teboulle, “A fast iterative shrinkage-thresholding algorithm for linear inverse problems,” *SIAM journal on imaging sciences*, vol. 2, no. 1, pp. 183–202, 2009.
- [52] P. L. Combettes and V. R. Wajs, “Signal recovery by proximal forward-backward splitting,” *Multiscale modeling & simulation*, vol. 4, no. 4, pp. 1168–1200, 2005.
- [53] J. Liu, S. Asif, B. Wohlberg, and U. Kamilov, “Recovery analysis for Plug-and-Play priors using the restricted eigenvalue condition,” in *Advances in Neural Information Processing Systems*, 2021.
- [54] A. Pramanik and M. Jacob, “Improved model based deep learning using monotone operator learning (mol),” in *2022 IEEE 19th International Symposium on Biomedical Imaging (ISBI)*, 2022, pp. 1–4.
- [55] T. Huster, C.-Y. J. Chiang, and R. Chadha, “Limitations of the Lipschitz constant as a defense against adversarial examples,” in *Joint European Conference on Machine Learning and Knowledge Discovery in Databases*. Springer, Cham, 2018, pp. 16–29.
- [56] C. Anil, J. Lucas, and R. Grosse, “Sorting out Lipschitz function approximation,” in *Proceedings of the 36th International Conference on Machine Learning*, ser. Proceedings of Machine Learning Research, vol. 97. PMLR, 2019, pp. 291–301.
- [57] S. Neumayer, A. Goujon, P. Bohra, and M. Unser, “Approximation of Lipschitz functions using deep spline neural networks,” *arXiv:2204.06233*, 2022.
- [58] K. Zhang, W. Zuo, Y. Chen, D. Meng, and L. Zhang, “Beyond a gaussian denoiser: Residual learning of deep CNN for image denoising,” *IEEE Transactions on Image Processing*, vol. 26, no. 7, pp. 3142–3155, 2017.
- [59] P. Arbeláez, M. Maire, C. Fowlkes, and J. Malik, “Contour detection and hierarchical image segmentation,” *IEEE Transactions on Pattern Analysis and Machine Intelligence*, vol. 33, no. 5, pp. 898–916, 2011.
- [60] A. Chambolle, “An algorithm for total variation minimization and applications,” *Journal of Mathematical imaging and vision*, vol. 20, no. 1, pp. 89–97, 2004.
- [61] F. Knoll, J. Zbontar, A. Sriram, M. J. Muckley, M. Bruno, A. Defazio, M. Parente, K. J. Geras, J. Katsnelson, H. Chandarana, Z. Zhang, M. Drozdalv, A. Romero, M. Rabbat, P. Vincent, J. Pinkerton, D. Wang, N. Yakubova, E. Owens, C. L. Zitnick, M. P. Recht, D. K. Sodickson, and Y. W. Lui, “fastMRI: A publicly available raw k-space and DICOM dataset of knee images for accelerated MR image reconstruction using machine learning,” *Radiology: Artificial Intelligence*, vol. 2, no. 1, 2020.
- [62] C. McCollough, “TU-FG-207A-04: Overview of the low dose CT grand challenge,” *Medical Physics*, vol. 43, no. 6Part35, pp. 3759–3760, 2016.
- [63] A. Beck and M. Teboulle, “Fast gradient-based algorithms for constrained total variation image denoising and deblurring problems,” *IEEE Transactions on Image Processing*, vol. 18, no. 11, pp. 2419–2434, 2009.
- [64] W. T. Freeman, E. H. Adelson *et al.*, “The design and use of steerable filters,” *IEEE Transactions on Pattern analysis and machine intelligence*, vol. 13, no. 9, pp. 891–906, 1991.
- [65] M. Unser and N. Chenouard, “A unifying parametric framework for 2d steerable wavelet transforms,” *SIAM Journal on Imaging Sciences*, vol. 6, no. 1, pp. 102–135, 2013.

before terminating. The proposed approach is predicated on the observation that the optimization landscape in the  $(\lambda, \mu)$  domain is typically well-behaved. The same principles apply to tune a single hyperparameter, which we used for the TV and the PnP- $\beta$ NN methods for instance. Remark: the performances were found to change only slowly with the scaling parameter  $\mu$  for the MRI and CT experiments. Hence, in practice, a very coarse tuning for  $\mu$  should suffice.

## APPENDIX

### A. Hyperparameter Tuning

The parameters  $\lambda$  and  $\mu$  used in (35) can be tuned with a coarse-to-fine approach. Given the performance on the  $3 \times 3$  grid  $\{(\gamma_\lambda)^{-1}\lambda, \lambda, \gamma_\lambda\lambda\} \times \{(\gamma_\mu)^{-1}\mu, \mu, \gamma_\mu\mu\}$ , we identify the best values  $\lambda^*$  and  $\mu^*$  on this subset and move on to the next iteration as follows:

- if  $\lambda^* = \lambda$ , the search grid is refined by reducing  $\gamma_\mu$  to  $(\gamma_\mu)^\zeta$ ,  $\zeta < 1$ ;
- otherwise,  $\lambda$  is updated to  $\lambda^*$ .

A similar update is performed for the scaling parameter. The search is terminated when both  $\gamma_\lambda$  and  $\gamma_\mu$  are smaller than a threshold, typically 1.01. In practice, we initialized  $\gamma_\lambda = \gamma_\mu = 4$  and set  $\zeta = 0.5$ . The method usually requires between 50 and 100 evaluations on tuples  $(\lambda, \mu)$  on the validation set